# World-wide InSAR sensitivity index for landslide deformation tracking

van Natijne, A.L.; Bogaard, T.A.; van Leijen, F.J.; Hanssen, R.F.; Lindenbergh, R.C.

**DOI**
10.1016/j.jag.2022.102829

**Publication date**
2022

**Document Version**
Final published version

**Published in**
International Journal of Applied Earth Observation and Geoinformation

International Journal of Applied Earth Observations and Geoinformation 111 (2022) 102829

Contents lists available at ScienceDirect

International Journal of Applied Earth Observations and Geoinformation

journal homepage: www.elsevier.com/locate/jag

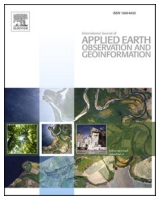

# World-wide InSAR sensitivity index for landslide deformation tracking

A.L. van Natijne [a,*], T.A. Bogaard [b], F.J. van Leijen [a], R.F. Hanssen [a], R.C. Lindenbergh [a]

[a] Department of Geoscience and Remote Sensing, Delft University of Technology, PO Box 5048, 2600GA Delft, the Netherlands
[b] Department of Water Management, Delft University of Technology, PO Box 5048, 2600GA Delft, the Netherlands

ARTICLE INFO

*Keywords:*
Landslides
Deformation tracking
InSAR
Sentinel-1
Sensitivity index

ABSTRACT

Landslides are a major geohazard in hilly and mountainous environments. In-situ inspection of downslope motion is costly, sometimes dangerous and, requires prior knowledge of the existence of a landslide. Remote sensing from space is a way to detect and characterize landslides systematically at large scale. Interferometric Synthetic Aperture Radar (InSAR) has shown to be a valuable resource of deformation information, but it requires expert knowledge and considerable computational efforts. Moreover, the successful application of InSAR for landslides requires a favorable acquisition geometry relative to the landslide deformation pattern. Consequently, there is a need for a widely applicable tool to assess the potential of InSAR at a particular location a priori. Here we present a novel, generic approach to assess the potential of InSAR-based deformation tracking, providing a standardised and automated method applicable on any slope. We define the detection potential as the sensitivity of InSAR to detect downslope displacement combined with the presence of coherently scattering surfaces. We show that deformation can be detected on at least 91% of the global landslide-prone slopes, and provide an open source Google Earth Engine tool for the quick assessment of the availability of potential coherent scatterers. This tool enables any person interested in applying InSAR to routinely assess the potential for monitoring landslide deformation in their region of interest.

## 1. Introduction

With an estimated average economic loss of € 4.7 billion per year in Europe alone, landslides are a major hazard (Haque et al., 2016). Knowledge of the landslide deformation behaviour provides insight in its characteristics and potential societal impact (Intrieri et al., 2019; van Natijne et al., 2020). Recent case studies show that satellite measurements of landslide deformation allow for the early detection of accelerated deformation preceding a catastrophic event (Intrieri et al., 2018; Carlá et al., 2019).

Several methods are available to obtain deformation measurements, each with different characteristics, temporal sampling, and spatial coverage. Local techniques include crackmeters, extensometers and inclinometers, that quantify in-situ deformation at the specific location at the landslide or building they are applied to (Logar et al., 2017; Segalini et al., 2019). Slope scale techniques, used to quantify differential deformation within a landslide, include total station measurements, and Global Navigation Satellite System (GNSS) measurement campaigns (Benoit et al., 2015). However, those techniques require access to the landslide for installation, maintenance and/or operation of sensors, reflectors or benchmarks.

Terrestrial laser scanning, photogrammetry and ground based radar are slope scale alternatives that can be deployed elsewhere, without access to the landslide, given free visibility of the landslide features (Jaboyedoff et al., 2012; Dewitte et al., 2008; Antonello et al., 2004). Aerial laser scanning and photogrammetric campaigns provide regional coverage, where especially laser scanning is able to penetrate vegetation on slopes. Deformation measurements can be based on feature tracking, as well as on a volumetric comparison of surface models (Zieher et al., 2019; Corsini et al., 2013). However, unless automated, all these measurements provide sparse, infrequent deformation measurements, that mask short-term variations in a long-term trend (Mansour et al., 2011).

Satellites provide an ideal platform for systematically repeating surveys over larger areas. Archives of wide scale acquisitions make it possible to detect previously unknown landslides and analyze historic landslide behaviour. Image-based correlation techniques are used for deformation tracking in both optical and radar amplitude imagery, tracking features in an image sequence over time (Mondini et al., 2019;

* Corresponding author.
*E-mail addresses:* A.L.vanNatijne@tudelft.nl (A.L. van Natijne), T.A.Bogaard@tudelft.nl (T.A. Bogaard), F.J.vanLeijen@tudelft.nl (F.J. van Leijen), R.F.Hanssen@tudelft.nl (R.F. Hanssen), R.C.Lindenbergh@tudelft.nl (R.C. Lindenbergh).

https://doi.org/10.1016/j.jag.2022.102829
Received 10 March 2022; Received in revised form 12 May 2022; Accepted 17 May 2022
Available online 6 June 2022

Singleton et al., 2014; Lacroix et al., 2018; Stumpf et al., 2017). However, their efficacy is limited to fast-moving landslides (Bickel et al., 2018). Furthermore, optical imagery is ineffective in case of cloud coverage.

These limitations are not applicable to deformation measurements obtained by satellite-borne Synthetic Aperture Radar Interferometry, InSAR (Hanssen, 2001). In less than two decades, InSAR has become an important information source for landslide deformation studies (Colesanti et al., 2003; Berardino et al., 2003; Hilley et al., 2004; Colesanti and Wasowski, 2006; Tofani et al., 2013), especially for slow to very slow landslides (0–1.6 m/year) (Hungr et al., 2014). These landslides can be tracked with coherent scatterers, natural or man-made reflectors that show phase-consistent scattering behaviour over time (Ferretti et al., 2001; Hanssen, 2001; Berardino et al., 2003; Komac et al., 2015).

InSAR studies consider a large variation in landslide types, processing techniques and objectives. Different deformation types include large scale block deformation (Czikhardt et al., 2017), rock slides (Lauknes et al., 2010; Delgado et al., 2011) and mud slides (Sun et al., 2015). Often, studies are local, and some studies validated InSAR results using field GPS measurements (Peyret et al., 2008; Yin et al., 2010; Komac et al., 2015). Regional studies, such as Aslan et al. (2020), are still rare, although continental scale InSAR products are under development (Crosetto et al., 2020). Others estimate landslide parameters based on InSAR time series in in-depth case studies (Intrieri et al., 2020; Schlögel et al., 2015).

Due to the numerous potential error sources, expert knowledge is required for the successful application of InSAR (van Leijen, 2014). In mountainous environments there is an additional effect on InSAR processing of the complex interaction with topography and the atmosphere (Hanssen, 2001). Furthermore, due the data heavy character of time series analysis, significant computational efforts are required. Therefore, it would be beneficial to be able to assess the applicability of InSAR before engaging in an in-depth study.

For this purpose, Cascini et al. (2009, 2010) introduced the concept of an InSAR 'visibility map' for landslides. However, it did not account for geometric distortion due to the effect of topography on the radar signal. An alternative 'feasibility index' was proposed by Notti et al. (2010). They proposed a surface geometry based method to estimate the likelihood of extracting deformation time series using InSAR, where feasibility was defined as the chance of the availability of a persistent scatterer in a series of SAR images. Their concept is implemented and extended in a range of later studies by Notti et al. (2011), Notti et al. (2014), Plank et al. (2010), Plank et al. (2012), Herrera et al. (2013), Cigna et al. (2013), Bianchini et al. (2013), Ciampalini et al. (2015), Novellino et al. (2017), Boní et al. (2020) and Del Soldato et al. (2021). However, the landslide deformation pattern was not incorporated.

Here we present a novel, comprehensive method to a priori assess the applicability of InSAR in landslide deformation detection at global scale. To be able to quantify the minimal detectable deformation (Teunissen, 2000; Baarda, 1968), we have adapted the sensitivity index (Chang et al., 2018) to the landslide process. The sensitivity index is available without prior knowledge of the deformation pattern or radar imagery, and is aimed at desk studies of the applicability of later InSAR landslide deformation analysis. Thanks to the sensitivity index, we could, for the first time, globally quantify the possibilities for InSAR slope monitoring.

Furthermore, we qualify the ability to extract deformation time series from the InSAR signal in a detection potential indicator. Finally, we provide a public detection potential tool in Google Earth Engine, that allows for an in-depth analysis of individual slopes. Together, these tools provide landslide experts, before engaging in an in-depth study, with a semi-automated assessment of the potential of landslide deformation tracking with InSAR.

In Section 2, we outline the principles of our method, followed by a detailed description of the calculation of the sensitivity index and detection potential indicator in Section 3. The tools accompanying this manuscript are demonstrated on a real world example in Section 4. Section 5 includes statistics on the global sensitivity index. Finally, we discuss the underlying assumptions in Section 6.

## 2. Defining InSAR measurement geometry

*Surface geometry.* Landslides are gravity induced and move downwards along the slope direction (Singleton et al., 2014). At a given time, the displacement of the landslide in the along-slope direction can be described by the instantaneous downslope or true velocity. The slope, $\beta$, is defined as the steepest downward direction, described by the aspect, $\alpha$, in clockwise degrees from north (0°– 360°). The slope steepness, $\beta$, is defined as the vertical angle from the horizontal.

A digital elevation model can be used to estimate the surface topography parameters, slope and aspect. Here we used the Copernicus DEM (Fahrland, 2020). The 30 m resolution at the equator is one of the highest for elevation models with (near) global coverage. The resolution impacts the representation accuracy of steep slopes, while the estimation of the aspect is less affected (Grohmann, 2015). For calculation convenience, flat slopes, i.e. $\beta \leqslant 5°$, are ignored in this study as the presence of a landslide system is expected to be extremely unlikely.

*Radar geometry.* The geometry of the InSAR acquisitions for a particular location is defined by the orientation of the line-of-sight (LOS) unit vector towards the satellite at the moment of imaging (Hanssen, 2001). Projected onto the horizontal plane, its angle from the north is referred to as the azimuth look direction (ALD), which is typically east-southeast for the descending (southbound) satellite orbit, and west-southwest for the ascending (northbound) orbit. The angle between the LOS unit vector and the zenith direction is referred to as the incidence angle, $\theta$, see Fig. 1, which is typically a value between $\theta_{min} = 29°$ and $\theta_{max} = 46°$ for Sentinel-1. Exact calculations are discussed in Section 3.1.

*Measurement geometry.* Key concept is the interaction between the radar geometry, surface geometry and landslide deformation. Two geometries inhibit proper interpretation of the radar signal: shadow and layover. In the case of shadow, the radar signal is blocked by topography. With layover, scatterers can no longer be unambiguously attributed to a single point on the Earth surface, as the radar signal scattered on multiple locations, at the same distance to the satellite, simultaneously and the signals are superimposed on each other. Fig. 1

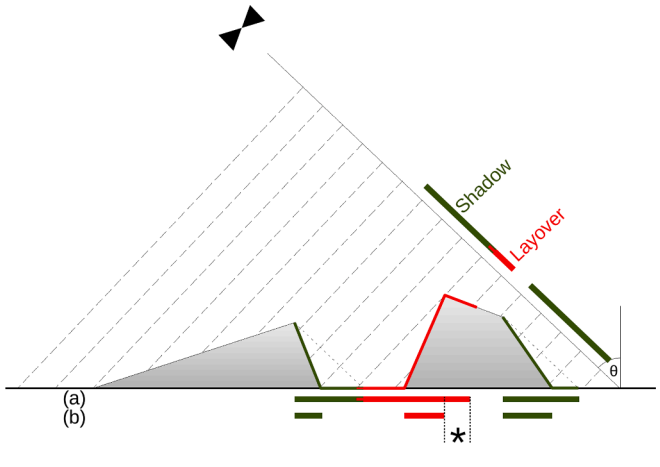


**Fig. 1.** Effects of surface topography on the radar image, shown in both the radar line-of-sight as the horizontal plane. The mapping from topography to line-of-sight is illustrated by the dashed lines, where the radar signal is simplified to a parallel wave front with incidence angle $\theta$. Under (a), the effects of surface topography on the radar image are shown mapped onto a DEM. Except for the area indicated by the asterisk, standard shadow algorithms in GIS are capable of modelling the destructive effects of topography on the radar signal. In comparison, (b) shows the effects that are locally detectable, without considering the surrounding surface topography, see Fig. 4. Image inspired by Pinel et al. (2014).

illustrates how these effects affect the radar acquisition in mountainous terrain.

To detect these effects in a 3D world, the apparent slope is a helpful variable. The apparent slope $\beta'$, is the slope as seen in the line-of-sight of the Sentinel-1 satellite:

$$\beta' = \beta \sin(\gamma' - \alpha), \tag{1}$$

with the terrain slope, $\beta$, aspect, $\alpha$, and satellite heading, $\gamma'$, corrected for meridian convergence. Fig. 3 illustrates the apparent slope in both ascending and descending orbits, for an artificial, radially symmetric mountain (Fig. 2).

Given the incidence angle, $\theta$, the geometric effects are found by simple relations: shadow occurs if $\beta' \leqslant -\theta$, layover occurs when $\beta' \geqslant 90^\circ - \theta$. These effects are illustrated in Fig. 4, for both the minimum and maximum incidence angle of Sentinel-1. However, on slope scale, as shown in Fig. 1, the effect of shadow and layover by neighbouring topography requires further modelling of the line-of-sight for an accurate representation.

## 3. Sensitivity index and detection potential

The application of InSAR deformation measurements is feasible when the following conditions are met: (i) the presence of coherent scatterers; and (ii) the availability of sufficient radar acquisitions with (iii) a geometry sensitive to deformation. Our work consists of two methods to assess these requirements (see Fig. 5). First we derive the sensitivity index, a static analysis of the lower bound of the sensitivity of Sentinel-1 to downslope deformation of the landslide. Second we define the detection potential indicator, which is a Google Earth Engine based tool to analyze the availability of imagery and scatterers from the Sentinel-1 time series contained in the Google Earth Engine archives.

*Definition of the sensitivity index.* Radar observations are only sensitive to deformation components in the propagation direction of the radar signal, the line-of-sight. Given the direction of downslope deformation, the sensitivity index, $s \in [0,1]$, is calculated by the orthogonal projection of the downslope unit vector onto the line-of-sight of the radar satellite (Chang et al., 2018). The most conservative incidence angle is used for the radar parameters, i.e. the incidence angle that yields the lowest sensitivity.

The sensitivity index is based on radar and surface geometry only, and the lower-bound is known without knowledge of the radar acquisitions. As such, the sensitivity index is a geometric property, that can be computed without the computational burden of downloading and processing large quantities of radar data. This index can be implemented in most Geographic Information Systems and is provided by us as a Google Earth Engine tool, and is a valuable assessment tool in the early planning phase.

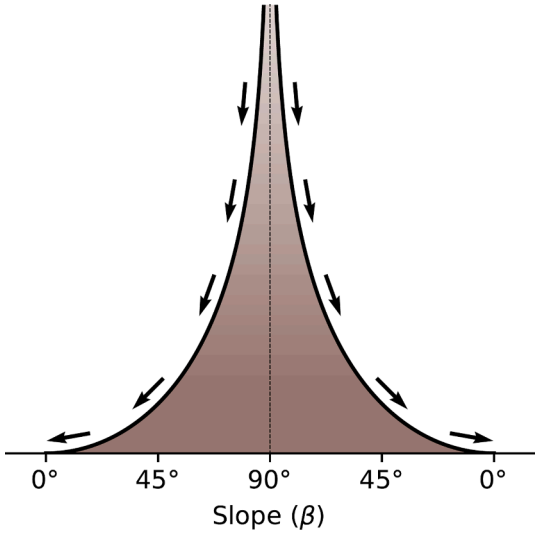


**Fig. 2.** Profile of a synthetic, radially symmetric mountain. The arrows indicate the expected sliding direction of a landslide.

*Definition of the detection potential.* The detection potential is quantified here by the estimated availability of presumedly coherent scatterers via the so-called method of normalized amplitude dispersion (Ferretti et al., 2001). Hereby, the amount of variability of the amplitude per radar-pixel in time is used as a proxy for the level of phase stability. Normalized amplitude dispersion is used by various InSAR packages as a convenient a priori selection technique for the selection of potential coherent scatterers (van Leijen, 2014). Although this method was originally aimed at coherent point scatterers, our application on multilooked and calibrated amplitude (GRD) instead of complex (SLC) data yields a proxy indication of coherent distributed scatterers as well. Only when a radar-pixel shows coherent scattering during a significant part of the full temporal extent, a displacement time series can be estimated. When the scatterer is disturbed or temporally obstructed, for example by snow, the scatterer (temporarily) loses coherence.

### 3.1. Sensitivity index algorithm

Starting point is the digital elevation model, from which the surface geometry is derived using standard functions available in most GIS packages (see Fig. 6). The surface geometry is derived from the DEM and combined with the radar geometry. On potential landslide slopes, the destructive geometric effects, shadow and layover, on the radar signal are estimated.

The system is operated on a tile basis, following the original 1° by 1° ($\sim 100 \times 100$ km) tiling of the Copernicus DEM data. The tiles can be merged into a regional or world map upon completion, as desired. Here we provide a detailed, step-by-step overview of the processing steps. Finally, we provide an analysis of the computational efficiency of the algorithm.

*Local Cartesian reference frame.* To ease calculations, a local Cartesian coordinate system is constructed for each DEM-pixel. Locally, the Earth is assumed to be spherical, with an apparent radius, $\rho(\phi)$, dependent on latitude $\phi$, estimated from the WGS84 ellipsoid underlying the Copernicus DEM. At pixel level, the Earth is assumed to be flat, and the curvature of the Earth with respect to its neighbours ignored. The apparent radius at latitude $\phi$ $[-90^\circ, 90^\circ]$ is given by (Husár et al., 2017):

$$\rho(\phi) = \frac{a\sqrt{1 - \frac{a^2-b^2}{a^2}}}{\sqrt{1 - \frac{a^2-b^2}{a^2}\cos^2(\phi)}} \tag{2}$$

with equatorial radius $a = 6378137$ meters and polar radius $b = 6356752$ meters. The resolution in $x$ and $y$, in meters, at latitude $\phi$ is then estimated as:

$$\begin{aligned} r_x(\phi) &\approx \rho(\phi) \cdot r_\lambda \cdot \cos(\phi), \\ r_y(\phi) &\approx \rho(\phi) \cdot r_\phi, \end{aligned} \tag{3}$$

with $r_\phi$ and $r_\lambda$ the latitudinal and longitudinal resolution in radians.

*Surface geometry.* The estimation of slope and aspect are based on the gradient calculation methods described by Horn (1981). These methods are the de facto standard for fast slope and aspect calculations in GIS (GDAL, GDAL/OGR contributors, 2020). The method is based on a weighted average of nearby pixels.

The neighbouring pixels in a $3 \times 3$ neighbourhood of elevations around $z_{0,0}$ are referenced to as follows:

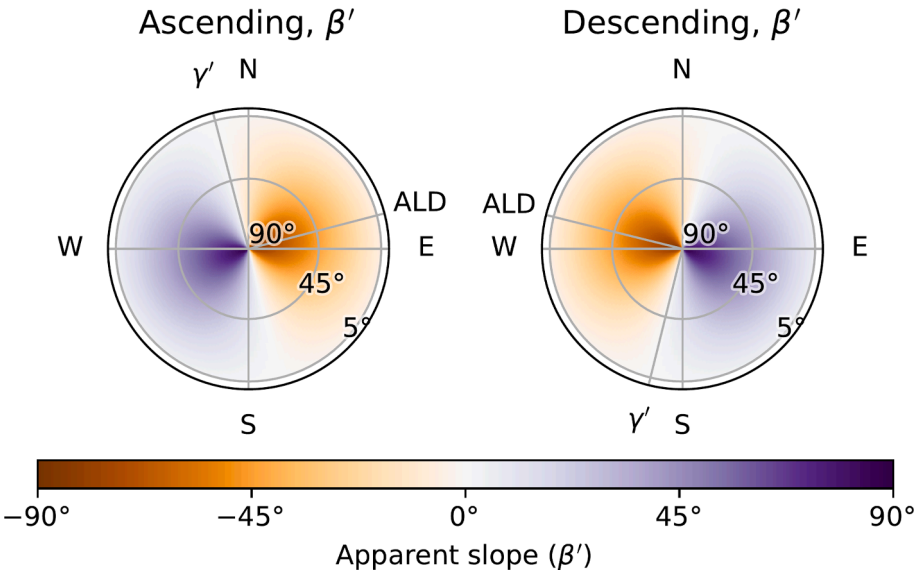


**Fig. 3.** Analysis of the apparent slope of an artificial, radially symmetric mountain, as illustrated in Fig. 2, at latitude $\phi \approx \pm 46°$. Fig. 4 shows a 2D schematization of the potential effects of surface geometry on the radar signal.

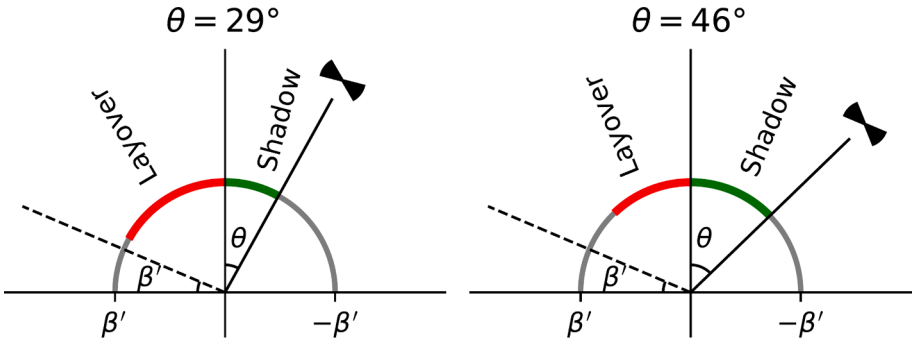


**Fig. 4.** 2D schematization of the effects of the surface geometry on the radar geometry. Illustrated are the minimum and maximum incidence angles $\theta$ of Sentinel-1 for a variable, apparent slope $\beta'$ $[-90°, 90°]$. Only the local effects, induced by the DEM-pixel itself, are described by these relations. Shadow or layover, induced by nearby topography, cf. Fig. 1 (b), cannot be captured this way.

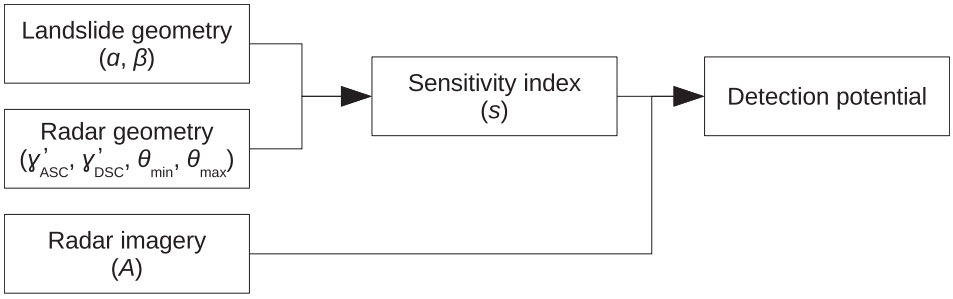


**Fig. 5.** An overview of the workflow and variables. Geometric analysis of the landslide and radar geometries (§2) leads to the sensitivity index for landslide deformation detection (§3.1). The detection potential (§3.2) is estimated by exploratory data analysis of archived radar imagery using Google Earth Engine.

$$\begin{array}{|c|c|c|} \hline z_{-1,-1} & z_{-1,0} & z_{-1,1} \\ \hline z_{0,-1} & z_{0,0} & z_{0,1} \\ \hline z_{1,-1} & z_{1,0} & z_{1,1} \\ \hline \end{array}. \tag{4}$$

The indices on the $y$-axis are inverted to match the convention on image coordinates, where the $y$-axis points down.

The weighted gradients in $x$-direction ($p$) and $y$-direction ($q$) are estimated as

$$\begin{aligned} p &= \frac{(z_{-1,1} + 2z_{0,1} + z_{1,1}) - (z_{-1,-1} + 2z_{0,-1} + z_{1,-1})}{8r_x(\phi)}, \\ q &= \frac{(z_{-1,1} + 2z_{-1,0} + z_{-1,-1}) - (z_{1,1} + 2z_{1,0} + z_{1,-1})}{8r_y(\phi)}. \end{aligned} \tag{5}$$

The gradients $p$ and $q$ yield a tangent, downslope vector, **t**,

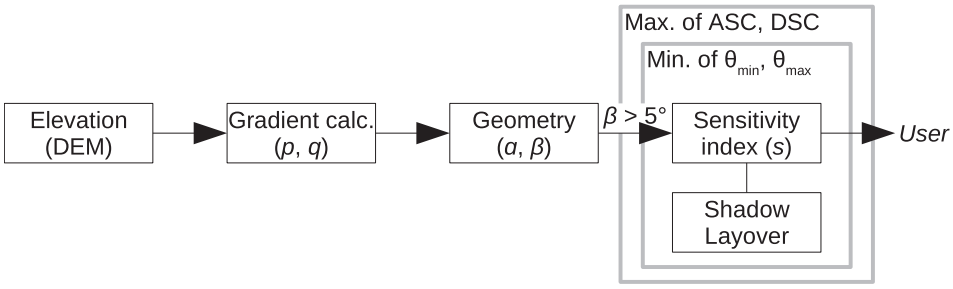


**Fig. 6.** Workflow for the calculation of the sensitivity index. The process is repeated for the two orbital directions, ascending and descending, and the extremes of the incidence angle ($\theta_{\min}, \theta_{\max}$). Result is a single value, the sensitivity index, the lower bound of the detectability of displacement in the radar signal. No radar imagery is required, only a digital elevation model and four orbit parameters.

$$\mathbf{t} = \frac{-1}{\sqrt{(1+p^2+q^2)(p^2+q^2)}} \begin{pmatrix} p \\ q \\ p^2+q^2 \end{pmatrix}. \tag{6}$$

If slope and aspect are already available, as in Google Earth Engine, the downslope vector may be constructed from them. With aspect $\alpha$ and slope $\beta$, the downslope vector is calculated as,

$$\mathbf{t} = \begin{bmatrix} \sin\alpha\cos\beta \\ \cos\alpha\cos\beta \\ -\sin\beta \end{bmatrix}. \tag{7}$$

*Radar geometry.* First, the effective heading of the satellite is estimated. The heading of the ascending orbit is approximated for latitude $\phi$ by Capderou (2005) as

$$\gamma'(\phi) \approx \arctan \frac{\cos i - \frac{\cos^2\phi}{\kappa}}{\sqrt{\cos^2\phi - \cos^2 i}}, \tag{8}$$

with $i$ the satellite inclination and $\kappa$ the mean motion, the number of revolutions per day. The effect of meridian convergence within the radar image is neglected. The heading of the descending orbit is $180° - \gamma'(\phi)$.

Similar to the downslope vector **t**, the vector for the satellite line-of-sight is constructed. The vector, **r**, points upward, from the Earth surface to the satellite. With satellite heading $\gamma'$, positive clockwise from the north, and $\theta$, the incidence angle from the vertical,

$$\mathbf{r} = \begin{bmatrix} -\cos\gamma'(\phi)\sin\theta \\ \sin\gamma'(\phi)\sin\theta \\ \cos\theta \end{bmatrix}. \tag{9}$$

*Shadow and layover.* The shadow and layover as derived from the apparent slope, shown in Figs. 4 and 3, represent only local effects, generated by the slope itself. However, as shown in Fig. 1, steep mountain slopes may affect larger regions on and at the foot of the slope. Following Cigna et al. (2013),Plank et al. (2012) and Cigna et al. (2012), we used a GIS-based shadow algorithm.

For the shadow estimation, the sun parameters are replaced with the satellite viewing geometry, $\gamma' + 90°$ from north and the maximum incidence angle ($\theta_{\max}$). For the layover estimate, the satellite is placed in opposite direction of $\gamma' - 90°$, at the minimum incidence angle ($\theta_{\min}$) from the horizontal. However, layover does not only affect the layover-inducing slope, but also areas above and below the slope, as shown in Fig. 1. This requires an extension to the shadow algorithm, where both the layover-inducing DEM-pixel as well as the DEM-pixel affected by the layover are marked.

For each DEM-pixel the line-of-sight to the radar is probed, until either obstructing topography is encounterd, or the maximum elevation in the tile is exceeded. If no obstructing topography is found, there is an unobstructed line-of-sight to the satellite.

*Sensitivity index.* The sensitivity index is, by definition, the projection of downslope deformation direction on the line-of-sight of the radar system (Chang et al., 2018):

$$s \doteq |\mathbf{t}\cdot\mathbf{r}|, \tag{10}$$

with downslope unit vector (**t**) from Eq. (6) or (7), and the line-of-sight unit vector (**r**) from Eq. (9). Where shadow or layover prevent radar measurements, the sensitivity index is set to zero.

Algebraic expressions exist for the two descriptions of the surface geometry. For the gradient method by Horn (1981), the sensitivity index is a combination of Eqs. (6), (9), and

$$s(p,q,\theta,\phi) = \frac{\left| \begin{pmatrix} (p^2+q^2)\cos(\theta) + \\ -p\cos(\gamma'(\phi)) + \\ q\sin(\gamma'(\phi)) \end{pmatrix} \sin(\theta) \right|}{\sqrt{p^2+q^2}\sqrt{p^2+q^2+1}}, \tag{11}$$

with satellite effective heading $\gamma'(\theta)$ and incidence angle $\theta$. Likewise, if the slope ($\beta$) and aspect ($\alpha$) are known instead of the gradients, a combination of Eqs. (7), (9) and (10) leads to:

$$s(\alpha,\beta,\theta,\phi) = |\sin(\beta)\cos(\theta) + \sin(\theta)\sin(\alpha - \gamma'(\phi))\cos(\beta)|. \tag{12}$$

The results are shown in Fig. 7 (a, b, d, e).

*Orbit aggregation.* The sensitivity index requires the exact incidence angle, see Eq. (9), that follows from actual InSAR data processing which is not available in the planning phase. Therefore, to include the unknown incidence angle in the planning, we conservatively use the minimum sensitivity from the two extremes of the incidence angle ($\theta_{\min}$, $\theta_{\max}$). The lowest sensitivity index found is a lower bound of the index for that slope, and can be quantified without knowledge of the exact orbits. This procedure is shown in Fig. 7 (a, f, g), and the final result is illustrated in 3D in Fig. 8.

For both the ascending and descending orbit, the minimum sensitivity index is taken, i.e.,

$$s_{asc} = \min(s_{\theta_{\min}}, s_{\theta_{\max}}). \tag{13}$$

Likewise, $s_{dsc}$ is calculated. The highest sensitivity index ($s$) of either ascending or descending orbit is the principal reporting parameter in the planning stage, when data from both ascending and descending orbit is expected to be available:

$$s \geqslant \max(s_{asc}, s_{dsc}). \tag{14}$$

*Landslide velocity.* The sensitivity index is defined as the projection of the downslope displacement unit vector onto the line-of-sight, and is a scale factor for the downslope displacement to the change in the line-of-sight range as observed by InSAR. For example, under the assumption of only downslope deformation, the downslope average velocity, $v_{\text{downslope}}$, is the line-of-sight average velocity, $v_{\text{LOS}}$, scaled by the sensitivity index, $s$,

$$v_{\text{downslope}} = \left| \frac{v_{\text{LOS}}}{s} \right|. \tag{15}$$

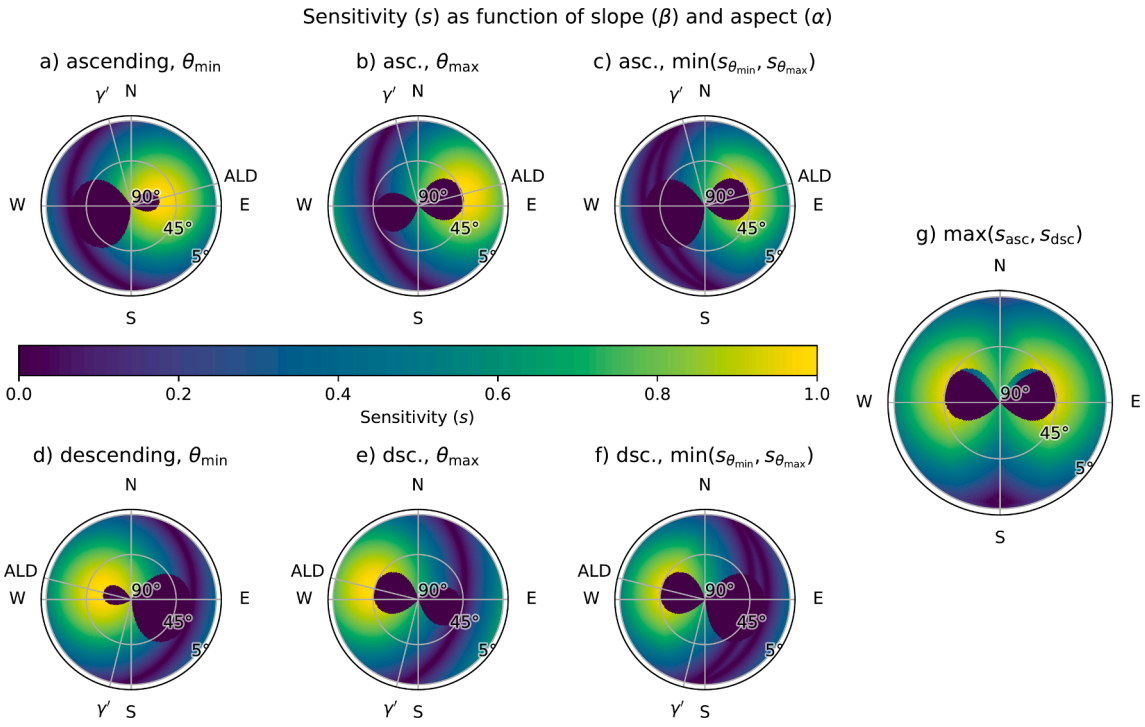


**Fig. 7.** The line-of-sight range sensitivity is expressed as a function of satellite and terrain parameters for latitude $\phi \approx \pm 46°$. The sensitivity is taken as the minimum sensitivity for the minimum and maximum incidence angle in order to provide conservative estimates. The effects of shadow and layover, as shown in Fig. 4, are resolved at DEM-pixel scale, therefore only the effects listed under (b) of Fig. 1 are resolved. Note that graph is based on an artificial, radial slope, as illustrated in Figs. 2 and 8, and does not represent a natural slope distribution. In practice, very steep slopes ($\geqslant 45°$) are rare, and comprise less than 1% of the slopes $> 5°$ in the Copernicus DEM.

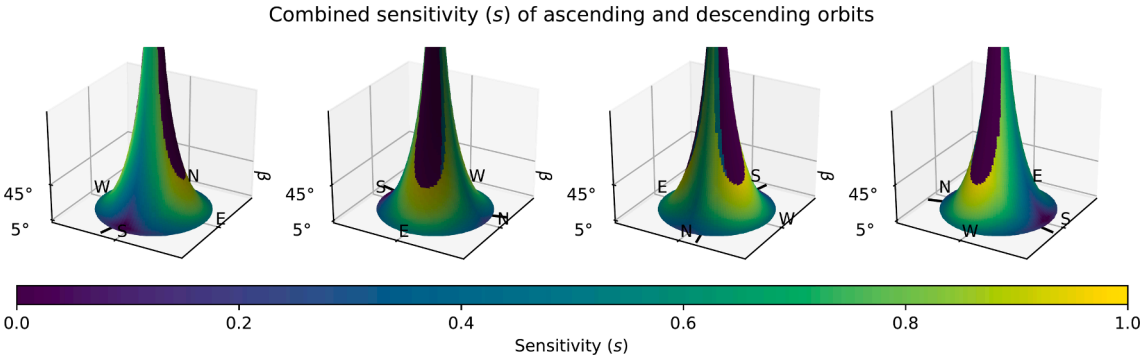


**Fig. 8.** A 3D interpretation of the results from Fig. 7. This image shows more clearly how shadow and layover affect only very steep slopes. Displacements along these slopes, as well as south facing, low relief slopes are less likely to be detectable. The ascending and descending orbit directions are shown in black at the bottom.

Likewise, via standard error propagation, the upper bound of the standard deviation may be found. In the case of a linear, average line-of-sight velocity:

$$\sigma_{v_{\text{downslope}}} = \frac{\sigma_{v_{\text{LOS}}}}{s} \text{ mm} \Big/ \text{yr}, \tag{16}$$

with $s$ and the expected standard deviation of the linear line-of-sight velocity $\sigma_{v_{\text{LOS}}}$. When the lower bound of the sensitivity index, as follows from Eq. (13), is used, Eqs. (15) and (16) provide estimates for their maximum values.

*Computational efficiency.* Computation of the sensitivity index for all 26 223 Copernicus DEM tiles required 13 hours on an Intel Xeon W-2123 (4 cores, 8 threads, 3.6 GHz) with 32 GB RAM and network storage. The sensitivity index was processed in Python (van Rossum, 2008) using Rasterio (Gillies et al., 2013), GeoPandas (Jordahl et al., 2020), GDAL (GDAL/OGR contributors, 2020), NumPy (Harris et al., 2020), and accelerated by Numba (Lam et al., 2015). Figures were generated using Matplotlib (Hunter, 2007). Thanks to the algebraic expressions, Eqs. (11) and (12), calculation of the sensitivity index for four cases (ascending/descending, $\theta_{\text{min}}/\theta_{\text{max}}$) is a trivial operation. However, the estimation of shadow and layover effects is more involved.

Our simple, iterative algorithm to compute the sensitivity index does not require cluster computing and is suitable for desktop computers due to its low memory footprint, that allows for parallel processing of multiple tiles. Moreover, the theoretical efficiency of $\mathcal{O}(n)$ is not indicative of the actual performance per tile. As flat areas are ignored, tiles over river deltas require very little computations. Tiles with large height differences are the most computationally intensive, as they require most iterations to resolve shadow and layover.

### 3.2. Detection potential algorithm

The estimation of the detection potential is an extension to the sensitivity index estimation, but now including a preliminary analysis of the available radar imagery. Moreover, the procedure, illustrated in Fig. 9, is implemented differently from the sensitivity index to match the structure of Google Earth Engine. In this structure, the algorithm is stored and evaluated in Google's data centers, where a 'multi-petabyte data catalog' and 'high-performance computing' facilities are co-located (Gorelick et al., 2017). Only once a portion of the map is requested, will the algorithm be evaluated for the region shown. The technology has proven to enable global analysis of decadal time series (Donchyts et al., 2016; Hansen and Loveland, 2012).

Google Earth Engine has an archive of Sentinel-1 GRD amplitude imagery available for processing. The availability of Sentinel-1 acquisitions enables us to use the actual incidence angle ($\theta$) to estimate the sensitivity index, rather than estimate the lower bound based on the theoretical range of the incidence angle. Unfortunately, the satellite heading ($\gamma'$) is not provided in or with the radar imagery, and is estimated by Eq. (8).

The Copernicus DEM was not available in Google Earth Engine at the time of writing. Instead, SRTM (Farr et al., 2007) is available, and is supplemented with ALOS DEM (Japan Aerospace Exploration Agency, 2019; Tadono et al., 2014) for higher latitudes. Predefined methods are available for the estimation of the surface geometry parameters, slope ($\beta$) and aspect ($\alpha$) (Google, 2021a). Due to computational limitations, a global analysis, such as with the global sensitivity index, is impossible.

Shadow and layover are approximated with a shadow model that takes single values for heading and incidence angle. This shadow model cannot be adapted to the incidence angle at DEM-pixel level, and a conservative value is taken instead. Furthermore, the shadow model is unable to detect layover in the region indicated by the asterisk in Fig. 1. On steep Alpine slopes, 6% of the pixels affected by layover stays undetected. However, this is just 0.02% of the total area of Alpine SRTM tile `N47E011`, that was tested as a sample.

*Normalized amplitude dispersion.* The normalized amplitude dispersion is defined as the ratio between the standard deviation of the amplitude, $\sigma_A$, and the mean amplitude, $\mu_A$, of a stack of radar images (Ferretti et al., 2001), applied on linear amplitude values:

$$D_A \doteq \frac{\sigma_A}{\mu_A}. \tag{17}$$

The normalized amplitude dispersion is a popular method for the initial selection of potentially coherent scatterers, as a low normalized amplitude dispersion is an indicator of high phase coherence (Ferretti et al., 2001). Thresholds for $D_A$ vary, depending on the application, between 0.25 and 0.6 (van Leijen, 2014; Hooper, 2008).

In Google Earth Engine only Ground Range Detected (GRD) imagery is available, that is a multi-looked (spatially averaged) amplitude derivative of the complex radar imagery (Google, 2021b). The use of the normalized amplitude dispersion on this type of imagery is unconventional, but is possible due to the radiometric consistency between the two products (Schubert and Small, 2016). However, as the multi-looking has a dampening effect on the amplitude dispersion, an area specific user interpretation of the normalized amplitude dispersion is recommended.

*Polarity.* Given the radar geometry for a specific orbit provided by Google Earth Engine, the effect of downslope displacement on the line-of-sight range may be estimated. The polarity ($\mathrm{sgn}(\mathbf{t}\cdot\mathbf{r}) \in \{-1, 0, +1\}$) indicates if downslope displacement is expected to shorten or lengthen the line-of-sight range. Together with the sensitivity index, the polarity enables preliminary estimates of the InSAR signal to be expected, based on prior knowledge of the specific slope. Moreover, spatial variability in the line-of-sight deformation direction could be misinterpreted for noise, but are not unlikely in mountainous topography.

*User interface.* In the Google Earth Engine tool, the detection potential is presented to the user as a filtered sensitivity index: the sensitivity index is shown whenever the normalized amplitude dispersion is below a threshold of 0.4. The application leaves three variables for the user to decide: (i) the orbit to analyze; (ii) the time span to analyze and (iii) the region of interest. First two parameters are offered to the user as selection boxes. The third is provided implicitly by moving around the map. Section 4.2 includes a demonstration of the application and associated user interface.

## 4. Global sensitivity index statistics and detection potential application

This study is accompanied by two tools: (i) the first global sensitivity index for landslide deformation detection by InSAR, and (ii) a Google Earth Engine tool for local analysis of the sensitivity index and detection potential. Both results are freely available to future users, either as data product, or as application and algorithm.

### 4.1. Global sensitivity index

The global sensitivity index, illustrated in Fig. 10, is available for download. Potential applications include combinations with regional landslide inventories or susceptibility maps, for example for monitoring planning. Tiling is equal to the tiling of the Copernicus DEM, and consists of 26 223 tiles of $1^\circ \times 1^\circ$. Each tile consists of three layers: $s_{asc}$; $s_{dsc}$ and $s$. The data is distributed as GeoTIFF, and is compatible with most common GIS software packages.

Sensitivity index values are stored as 16 bit floats, with a variable longitude resolution, matching the variation of the Copernicus DEM. Flat regions, including water, as well as gaps in the data are marked as no data. The global tile set is only 330 GiB in size, with individual tiles ranging between 50 kiB and 90 MiB. Moreover, the associated algorithm is available.

The global sensitivity index and Python code are available for download via doi:10.4121/14095777, Natijne et al. (2021).

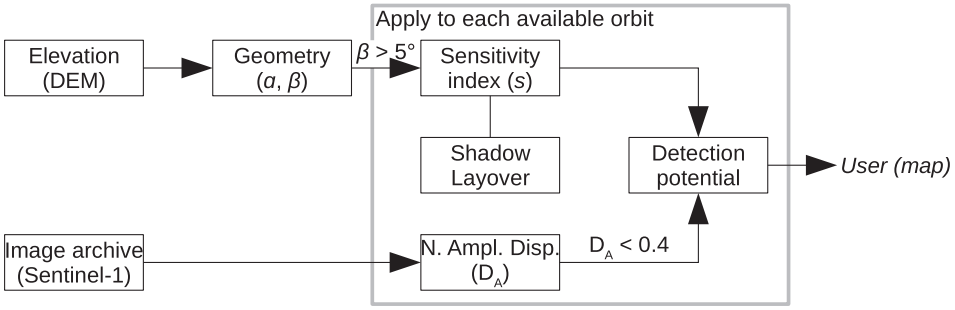


**Fig. 9.** InSAR detection potential is defined as the product of the sensitivity index, shadow and layover, as well as scattering characteristics estimated from imagery. The application of InSAR is only feasible in the presence of unobstructed scattering surfaces on slopes with a sufficient sensitivity index for the expected landslide velocity.

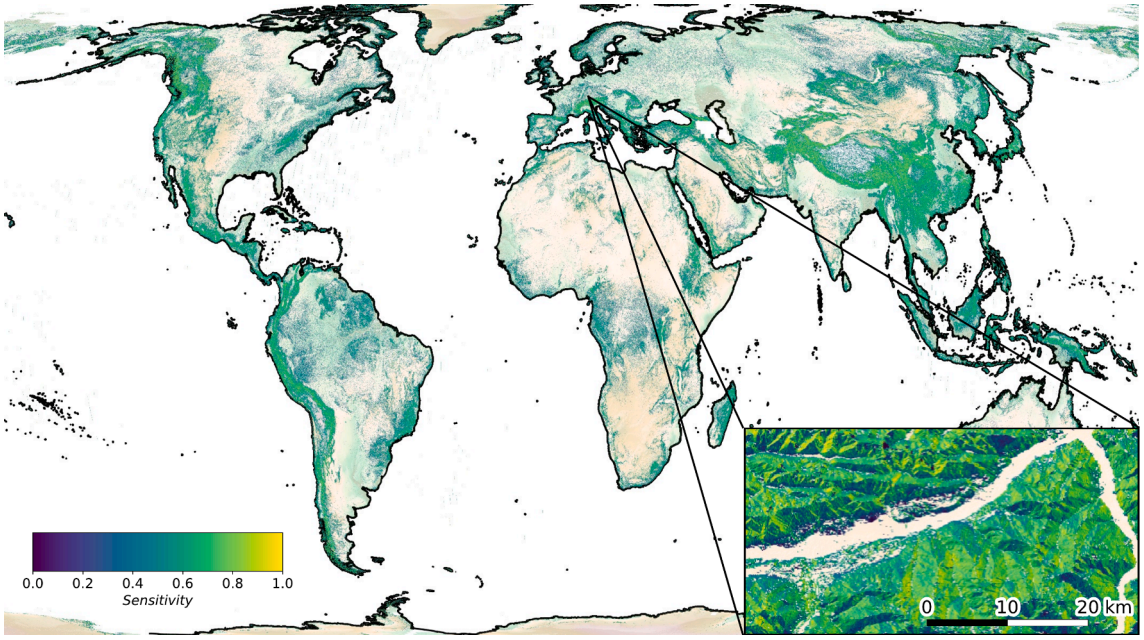


**Fig. 10.** Global sensitivity index and an excerpt over the Inn valley, around Innsbruck, Austria. Shown is the combined sensitivity index, the highest sensitivity from the conservative, lower-bound, estimates of the sensitivity index for the ascending and descending orbits. The index is available globally, at around 30 m resolution. (Background: Copernicus DEM and OpenStreetMap coastlines).

### *4.2. Sensitivity index and detection potential in Google Earth Engine*

The Google Earth Engine tool allows the user for a more detailed study of in the sensitivity index and detection potential in their area of interest. At a regional level, the sensitivity index is shown (Fig. 12). Locally, the application will search the Google Earth Engine archives for available Sentinel-1 imagery in the desired time frame and offer the user a sensitivity index tailored to an orbit of choice. Furthermore, at slope level, the detection potential indicator can be used to highlight the sensitivity index for potential coherent scatterers.

The Vögelsberg slope, near Innsbruck, Austria, is affected by a deep-seated landslide (Zieher et al., 2019; Pfeiffer et al., 2021). The steep valley shape as well as the various orientations of the surrounding slopes make it a complex setting for the application of InSAR analysis. Fig. 13, for example, shows the spatial variability in the effect of downslope displacement on the line-of-sight range. Fig. 14 shows the sensitivity index, and detection potential indicator for the region around the slope, as well as the detection potential indicator on the slope scale. Contrary to Fig. 12, that showed the lower bound of the sensitivity index, the sensitivity index in Fig. 14 is calculated based on the specific orbit parameters.

Using the Google Earth Engine tool, the user may explore the properties of the different orbits available. On the Vögelsberg landslide, where ground truth velocity estimates are available, not only the sign, but also the approximate magnitude of the average line-of-sight velocity is available via the sensitivity index (Eq. (15)). The various layers show not only the sensitivity index, but also the number of images available in each time frame and orbit. Especially with some prior knowledge of the landslide deformation pattern, the orbit with suitable coverage of the expected displacement can be found.

The Google Earth Engine tool is available on: https://avannatijne.users.earthengine.app/view/landslide-insar.

## 5. Results of the global sensitivity index

A statistical analysis of the global sensitivity index is shown in Fig. 11. These numbers are aggregated statistics of all slopes in the Copernicus DEM, corrected for the reduced DEM-pixel size towards the poles. Notti et al., 2014 suggested that, as rule of thumb, landslides with a sensitivity index greater than 0.2 allow for deformation monitoring by

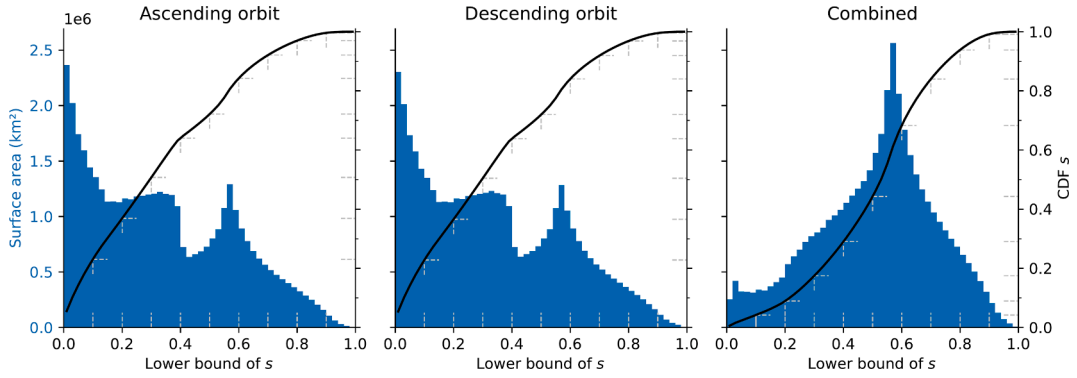


**Fig. 11.** Histograms of computed global sensitivity index values, for both ascending and descending orbits, as well as the highest sensitivity index from either orbit. Included are all slopes mapped by the Copernicus DEM, steeper than 5°. Areas invisible due to layover or shadow are marked as 0 sensitivity. The cumulative distribution function of the absolute value of the lower bound of sensitivity, is given in black.

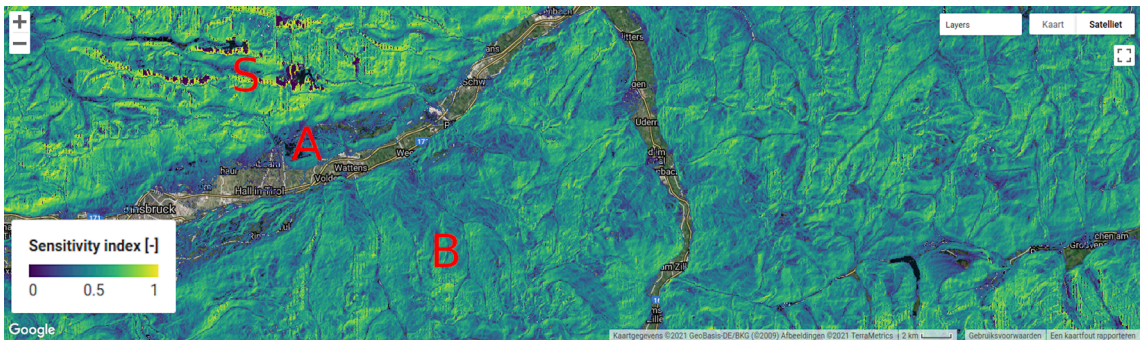


**Fig. 12.** Example of the sensitivity index, as generated in Google Earth Engine, for part of the Inn valley, around Innsbruck and Wattens, Tirol, Austria. The valley is flat, at a slope of less than 5°, and reveals the underlying map. Small patches in the north-west, marked 'S' in the image, are shown as dark blue, indicating no sensitivity to deformation due to either shadow, layover or a combination of both. The south-east facing slopes on the northern side of the Inn valley, 'A', suffer from poor sensitivity. Therefore, only strong displacement signals will be detectable here, if at all. Side valleys in the south-east, of the image, at 'B', show more gradual topography and typically high sensitivity. As the highest sensitivity index value of either the ascending or descending orbit is reported, both east and west facing slopes are marked visible in this image. Note that the sensitivity index is higher on slopes facing north than on south-facing slopes. (Map: Google Earth Engine).

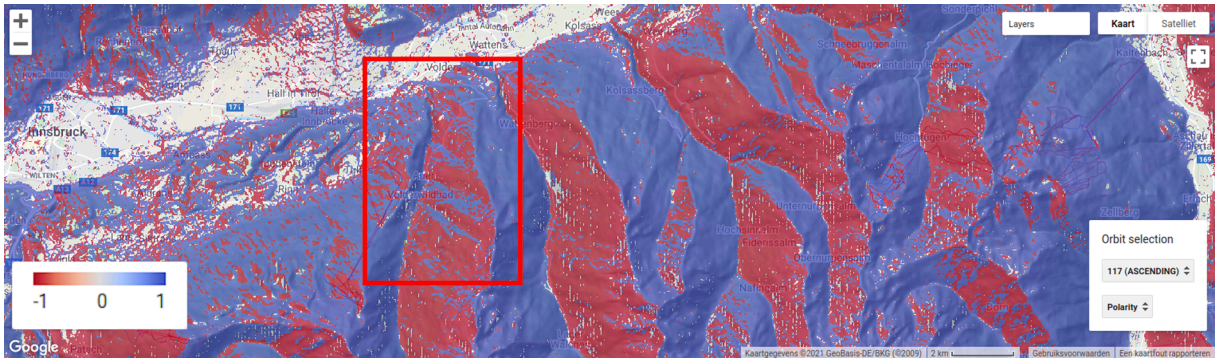


**Fig. 13.** Example of polarity product in Google Earth Engine. The area, marked by the red rectangle, is the Großvolderberg, near Innsbruck, Tirol, Austria. This slope shows how, even in a small area, downslope deformation will be represented by a mix of lengthening ( $+1$) and shortening ( $-1$) in the InSAR data. Prior knowledge of the polarity will aid the interpretation of the InSAR signal, that may appear noisy due to frequent sign changes within slopes. (Map: Google Earth Engine).

InSAR. Based on this threshold, the global sensitivity index shows that displacement of at least 91% of the world's slopes would be observable by InSAR. If only a single orbit is available at a given location, either ascending or descending, 64% of the slopes is within this criterion. Our results for the individual orbit directions are in line with Novellino et al. (2017), who concluded that 67.2% of Great-Britain could be observed in an ascending orbit and 67.5% in a descending orbit.

## 6. Discussion

Various assumptions underpin our proposed methodology, allowing us to evaluate the sensitivity index globally and integrate the detection potential in Google Earth Engine as products that do not require expert knowledge and experience to operate.

*Landslide behaviour.* In the absence of information on the landslide type, in this study, a principal assumption is that landslides undergo downslope displacement only (Bianchini et al., 2013; Singleton et al., 2014). Although most landslide types undergo at least some form of downslope deformation, different parts of the landslide may move in different directions, such as uplift at the toe of a rotational landslide, or thinning at the scar of translational slides (Frattini et al., 2018). Schlögel et al. (2015) even suggest that vertical deformation signals, due to subsidence at the scarp and accumulation at the toe, are stronger than downslope deformation. Furthermore, basal sliding will follow the slope of the slip surface rather than the surface topography (Massey et al., 2013). If the landslide type is known, and a specific deformation pattern is expected, the sensitivity index can be adapted to include deformation in any direction (e.g. in case of subsidence: $\mathbf{r} = [0 \quad 0 \quad -1]^{\mathrm{T}}$).

*Radar geometry.* Thanks to the Copernicus program, there is and will be an abundant availability of Sentinel-1 imagery. Therefore, the focus of this paper in on Sentinel-1 data. However, there is no full coverage of the Earth with both ascending and descending orbits (Copernicus Space Component Mission Management Team, 2019). As a consequence, the global sensitivity index may overestimate the sensitivity index in areas covered by only a single orbital direction.

The methodology could just as well be applied to any other satellite or satellite constellation. This method is already effective with knowledge of only three to four acquisition parameters: extremes of the incidence angle: $\theta_{\min}$, $\theta_{\max}$; satellite orbit parameters: inclination $i$ and mean motion $\kappa$ in revolutions per day. For TerraSAR-X, for example: $\theta_{\min} = 20°$, $\theta_{\max} = 45°$, $i = 97.44°$ and $\kappa = 15.1914$ (Airbus Defence and Space, 2015).

*Time series.* All images are assumed to be usable for time series analysis. In practice, images might be missing or unusable due to anomalies (e.g. long baselines) or seasonal effects (e.g. snow cover). Long periods without observation may trigger unwrapping errors as well as increase the minimum significant detectable landslide velocity. Furthermore, significant changes in scattering characteristics will spoil the coherence of the scatterers fundamental to InSAR. Snow and flooding alter scattering characteristics temporarily and potentially permanently, leading to the loss of the time series.

The maximum landslide deformation resolvable from interferometric phase differences is limited by the wavelength as well as the gradient between neighbouring observations in space and time. Under ideal circumstances, without noise, this so-called unwrapping limit for independent observations is a quarter of the wavelength $\lambda$ of the radar

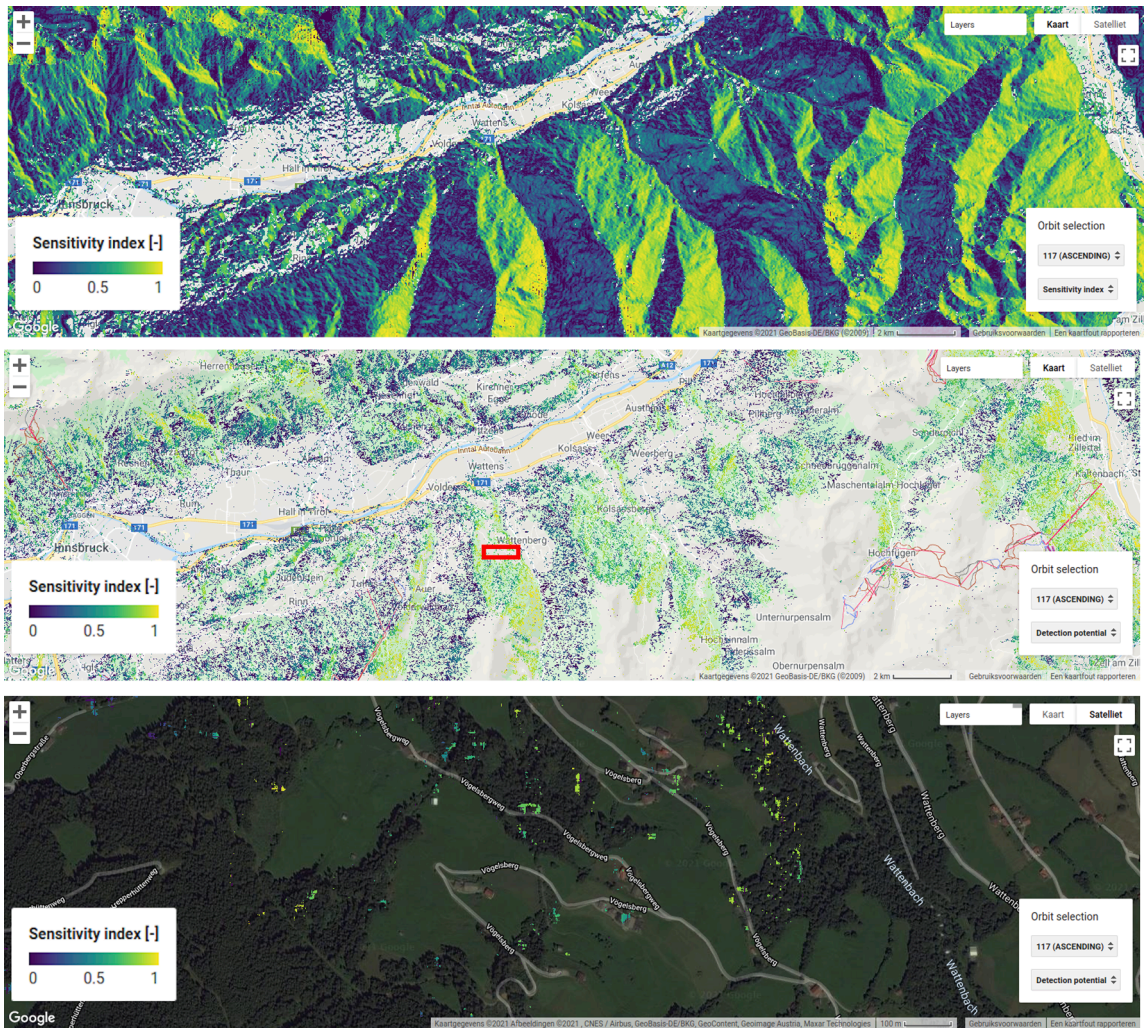


**Fig. 14.** Three maps over the Inn valley, as generated by our Google Earth Engine tool. Coverage for the top two images is identical to Fig. 12: the Inn valley around Innsbruck and Wattens, Tirol, Austria. Top: the sensitivity index, with the radar geometry specific for ascending orbit 117 of Sentinel-1. Very few areas are invisible to the radar (dark blue). Flat areas, such as the Inn valley, where the slope is less than 5°, are transparent and show the underlying map. Center: The sensitivity index, masked by the detection potential, shows the sensitivity where the normalized amplitude dispersion is not greater than 0.4. Except for the high mountain ridges, the lower part of the slopes show patches of potential coherent scatterers, and are more likely to have a successful application of InSAR. Bottom: An excerpt of the previous map, marked by the red rectangle. This map shows the sensitivity index, again masked by the detection potential: a normalized amplitude dispersion not greater than 0.4. The map shows a high likelihood of finding coherent scatterers on/around the houses, while for fields an actual InSAR data processing procedure would be required to assess the actual coherence level. Forest pixels are unlikely candidates, but have a sufficiently low normalized amplitude dispersion due to their consistent, low amplitude. (Map: Google Earth Engine).

system: $\pm\frac{\lambda}{4}$. However, this assumption is too rigorous. First, especially on slopes with a low sensitivity $s$, the effective limit on deformation will be much larger: $\pm\frac{\lambda}{4s}$. Second, neighbouring observations on the landslide, that underwent less deformation since the last acquisition, may provide a spatial gradient of resolvable differences. Finally, under the assumption of downslope deformation only, the unwrapping limit may be expanded to half the wavelength: $\frac{\lambda}{2s}$.

## 7. Conclusions

Analysis of our global sensitivity index indicated that at least 91% of the global slopes are likely to allow for InSAR deformation monitoring with Sentinel-1. The Google Earth Engine tool provides an initial, local analysis of the available radar imagery, and highlights areas with potentially favourable scattering characteristics. Together, the sensitivity index and detection potential indicator provide an a priori indicator of the likelihood of success of InSAR campaigns. Therefore, they are valuable tools in the planning phase of an InSAR campaign, where the Google Earth Engine tool accelerates the initial site survey and orbit selection process, while the global sensitivity index extends landslide inventories, hazard or susceptibility maps with an indication of the InSAR monitoring potential. The methodology presented is easily extended to other satellite constellations and/or deformation patterns.

The global sensitivity index is available for download via doi:10.4121/14095777, the Google Earth Engine tool is available on `https://avannatijne.users.earthengine.app/view/landslide-insar`. Underlying code is available with their products.

## CRediT authorship contribution statement

**A.L. van Natijne**: Methodology, Software, Writing – original draft. **T.A. Bogaard**: Supervision, Writing – review & editing. **F.J. van Leijen**: Writing – review & editing. **R.F. Hanssen**: Conceptualization, Writing – review & editing. **R.C. Lindenbergh**: Supervision, Writing – review & editing.

## Declaration of Competing Interest

The authors declare that they have no known competing financial interests or personal relationships that could have appeared to influence the work reported in this paper.

## Acknowledgements

This work was carried out under the framework of the OPERANDUM (OPEn-air laboRAtories for Nature baseD solUtions to Manage hydro-meteo risks) project, which is funded by European Union's Horizon 2020 Framework Programme for research and innovation under grant agreement 776848.

## References

Airbus Defence and Space, 2015. TerraSAR-X image product guide. URL: https://www.intelligence-airbusds.com/files/pmedia/public/r459_9_20171004_tsxx-airbusds-ma-0009_tsx-productguide_i2.01.pdf. technical report.

Antonello, G., Casagli, N., Farina, P., Leva, D., Nico, G., Sieber, A.J., Tarchi, D., 2004. Ground-based SAR interferometry for monitoring mass movements. Landslides 1, 21–28. https://doi.org/10.1007/s10346-003-0009-6. URL: http://link.springer.com/10.1007/s10346-003-0009-6.

Aslan, G., Foumelis, M., Raucoules, D., De Michele, M., Bernardie, S., Cakir, Z., 2020. Landslide mapping and monitoring using Persistent Scatterer Interferometry (PSI) technique in the French alps. Remote Sens. 12, 1305. https://doi.org/10.3390/rs12081305. URL: https://www.mdpi.com/2072-4292/12/8/1305.

Baarda, W., 1968. A testing procedure for use in geodetic networks, Publications on geodesy, second ed., , vol. 5, Netherlands Geodetic Commission, Delft.

Benoit, L., Briole, P., Martin, O., Thom, C., Malet, J.P., Ulrich, P., 2015. Monitoring landslide displacements with the Geocube wireless network of low-cost GPS. Eng. Geol. 195, 111–121. https://doi.org/10.1016/j.enggeo.2015.05.020. URL: https://linkinghub.elsevier.com/retrieve/pii/S001379521500174X.

Berardino, P., Costantini, M., Franceschetti, G., Iodice, A., Pietranera, L., Rizzo, V., 2003. Use of differential SAR interferometry in monitoring and modelling large slope instability at Maratea (Basilicata, Italy). Eng. Geol. 68, 31–51. https://doi.org/10.1016/S0013-7952(02)00197-7. URL: https://linkinghub.elsevier.com/retrieve/pii/S0013795202001977.

Bianchini, S., Herrera, G., Mateos, R., Notti, D., Garcia, I., Mora, O., Moretti, S., 2013. Landslide Activity Maps Generation by Means of Persistent Scatterer Interferometry. Remote Sens. 5, 6198–6222. https://doi.org/10.3390/rs5126198. URL: http://www.mdpi.com/2072-4292/5/12/6198.

Bickel, V., Manconi, A., Amann, F., 2018. Quantitative assessment of digital image correlation methods to detect and monitor surface displacements of large slope instabilities. Remote Sens. 10, 865. https://doi.org/10.3390/rs10060865. URL: http://www.mdpi.com/2072-4292/10/6/865.

Boní, R., Bordoni, M., Vivaldi, V., Troisi, C., Tararbra, M., Lanteri, L., Zucca, F., Meisina, C., 2020. Assessment of the Sentinel-1 based ground motion data feasibility for large scale landslide monitoring. Landslides 17, 2287–2299. https://doi.org/10.1007/s10346-020-01433-3. URL: http://link.springer.com/10.1007/s10346-020-01433-3.

Capderou, M., 2005. Satellites, orbits and missions. Springer-Verlag, Paris. doi:10.1007/b139118. URL: http://link.springer.com/10.1007/b139118.

Carlá, T., Intrieri, E., Raspini, F., Bardi, F., Farina, P., Ferretti, A., Colombo, D., Novali, F., Casagli, N., 2019. Perspectives on the prediction of catastrophic slope failures from satellite InSAR. Sci. Rep. 9 https://doi.org/10.1038/s41598-019-50792-y. URL: http://www.nature.com/articles/s41598-019-50792-y.

Cascini, L., Fornaro, G., Peduto, D., 2009. Analysis at medium scale of low-resolution DInSAR data in slow-moving landslide-affected areas. ISPRS J. Photogramm. Remote Sens. 64, 598–611. https://doi.org/10.1016/j.isprsjprs.2009.05.003. URL: https://linkinghub.elsevier.com/retrieve/pii/S0924271609000628.

Cascini, L., Fornaro, G., Peduto, D., 2010. Advanced low- and full-resolution DInSAR map generation for slow-moving landslide analysis at different scales. Eng. Geol. 112, 29–42. https://doi.org/10.1016/j.enggeo.2010.01.003. URL: https://linkinghub.elsevier.com/retrieve/pii/S0013795210000049.

Chang, L., Dollevoet, R.P.B.J., Hanssen, R.F., 2018. Monitoring Line-Infrastructure With Multisensor SAR Interferometry: Products and Performance Assessment Metrics. IEEE J. Sel. Top. Appl. Earth Observ. Remote Sens. 11, 1593–1605. https://doi.org/10.1109/JSTARS.2018.2803074. URL: https://ieeexplore.ieee.org/document/8306273/.

Ciampalini, A., Raspini, F., Bianchini, S., Frodella, W., Bardi, F., Lagomarsino, D., Di Traglia, F., Moretti, S., Proietti, C., Pagliara, P., Onori, R., Corazza, A., Duro, A., Basile, G., Casagli, N., 2015. Remote sensing as tool for development of landslide databases: The case of the Messina Province (Italy) geodatabase. Geomorphology 249, 103–118. https://doi.org/10.1016/j.geomorph.2015.01.029. URL: https://linkinghub.elsevier.com/retrieve/pii/S0169555X15000586.

Cigna, F., Bateson, L., Colm, J., Dashwood, C., 2013. Nationwide monitoring of geohazards in Great Britain with InSAR: Feasibility mapping based on ERS-1/2 and ENVISAT imagery. In: 2013 IEEE International Geoscience and Remote Sensing Symposium - IGARSS, IEEE, Melbourne, Australia. pp. 672–675. doi:10.1109/IGARSS.2013.6721246. URL: http://ieeexplore.ieee.org/document/6721246/.

Cigna, F., Bateson, L.B., Jordan, C.J., Dashwood, C., 2012. Feasibility of InSAR technologies for nationwide monitoring of geohazards in Great Britain. In: Proceedings of the Remotesensing and Photogrammetry Society Conference 2012, RSPSoc, University of Greenwich, London. URL: http://nora.nerc.ac.uk/id/eprint/19876/.

Colesanti, C., Ferretti, A., Prati, C., Rocca, F., 2003. Monitoring landslides and tectonic motions with the Permanent Scatterers Technique. Eng. Geol. 68, 3–14. https://doi.org/10.1016/S0013-7952(02)00195-3. URL: https://linkinghub.elsevier.com/retrieve/pii/S0013795202001953.

Colesanti, C., Wasowski, J., 2006. Investigating landslides with space-borne Synthetic Aperture Radar (SAR) interferometry. Eng. Geol. 88, 173–199. https://doi.org/10.1016/j.enggeo.2006.09.013. URL: https://linkinghub.elsevier.com/retrieve/pii/S001379520600250X.

Copernicus Space Component Mission Management Team, 2019. Sentinel High Level Operations Plan (HLOP). URL: https://sentinels.copernicus.eu/documents/247904/685154/Sentinel_High_Level_Operations_Plan. technical report.

Corsini, A., Castagnetti, C., Bertacchini, E., Rivola, R., Ronchetti, F., Capra, A., 2013. Integrating airborne and multi-temporal long-range terrestrial laser scanning with total station measurements for mapping and monitoring a compound slow moving rock slide: monitoring rock slides by multi-temporal terrestrial laser scanning. Earth Surface Processes Landforms 38, 1330–1338. https://doi.org/10.1002/esp.3445. URL: http://doi.wiley.com/10.1002/esp.3445.

Crosetto, M., Solari, L., Mróz, M., Balasis-Levinsen, J., Casagli, N., Frei, M., Oyen, A., Moldestad, D.A., Bateson, L., Guerrieri, L., Comerci, V., Andersen, H.S., 2020. The evolution of wide-area DInSAR: from regional and national services to the European ground motion service. Remote Sens. 12, 2043. https://doi.org/10.3390/rs12122043. URL: https://www.mdpi.com/2072-4292/12/12/2043.

Czikhardt, R., Papco, J., Bakon, M., Liscak, P., Ondrejka, P., Zlocha, M., 2017. Ground stability monitoring of undermined and landslide prone areas by means of Sentinel-1 multi-temporal InSAR, case study from Slovakia. Geosciences 7, 87. https://doi.org/10.3390/geosciences7030087. URL: http://www.mdpi.com/2076-3263/7/3/87.

Del Soldato, M., Solari, L., Novellino, A., Monserrat, O., Raspini, F., 2021. A New Set of Tools for the Generation of InSAR Visibility Maps over Wide Areas. Geosciences 11, 229. https://doi.org/10.3390/geosciences11060229. URL: https://www.mdpi.com/2076-3263/11/6/229.

Delgado, J., Vicente, F., García-Tortosa, F., Alfaro, P., Estévez, A., Lopez-Sanchez, J., Tomás, R., Mallorquí, J., 2011. A deep seated compound rotational rock slide and rock spread in SE Spain: structural control and DInSAR monitoring. Geomorphology 129, 252–262. https://doi.org/10.1016/j.geomorph.2011.02.019. URL: https://linkinghub.elsevier.com/retrieve/pii/S0169555X11000833.

Dewitte, O., Jasselette, J.C., Cornet, Y., Van Den Eeckhaut, M., Collignon, A., Poesen, J., Demoulin, A., 2008. Tracking landslide displacements by multi-temporal DTMs: A combined aerial stereophotogrammetric and LiDAR approach in western Belgium. Eng. Geol. 99, 11–22. https://doi.org/10.1016/j.enggeo.2008.02.006. URL: https://linkinghub.elsevier.com/retrieve/pii/S0013795208000446.

Donchyts, G., Baart, F., Winsemius, H., Gorelick, N., Kwadijk, J., van de Giesen, N., 2016. Earth's surface water change over the past 30 years. Nat. Clim. Change 6, 810–813. https://doi.org/10.1038/nclimate3111. URL: http://www.nature.com/articles/nclimate3111.

Fahrland, E., 2020. Copernicus Digital Elevation Model. URL: https://spacedata.copernicus.eu/documents/20126/0/GEO1988-CopernicusDEM-SPE-002_ProductHandbook_I1.00+%281%29.pdf/40b2739a-38d3-2b9f-fe35-1184ccd17694?t=1612269439996. product handbook.

Farr, T.G., Rosen, P.A., Caro, E., Crippen, R., Duren, R., Hensley, S., Kobrick, M., Paller, M., Rodriguez, E., Roth, L., Seal, D., Shaffer, S., Shimada, J., Umland, J., Werner, M., Oskin, M., Burbank, D., Alsdorf, D., 2007. The Shuttle Radar Topography Mission. Rev. Geophys. 45 https://doi.org/10.1029/2005RG000183. URL: http://doi.wiley.com/10.1029/2005RG000183.

Ferretti, A., Prati, C., Rocca, F., 2001. Permanent scatterers in SAR interferometry. IEEE Trans. Geosci. Remote Sens. 39, 8–20. https://doi.org/10.1109/36.898661. URL: http://ieeexplore.ieee.org/document/898661/.

Frattini, P., Crosta, G.B., Rossini, M., Allievi, J., 2018. Activity and kinematic behaviour of deep-seated landslides from PS-InSAR displacement rate measurements. Landslides 15, 1053–1070. https://doi.org/10.1007/s10346-017-0940-6. URL: http://link.springer.com/10.1007/s10346-017-0940-6.

GDAL/OGR contributors, 2020. GDAL/OGR Geospatial Data Abstraction software Library. URL: https://gdal.org. software package.

Gillies, S. et al., 2013. Rasterio: geospatial raster I/O for Python programmers. URL: https://github.com/mapbox/rasterio. software package.

Google, 2021a. Google Earth Engine, ee.Algorithms.Terrain. URL: https://developers.google.com/earth-engine/apidocs/ee-algorithms-terrain.

Google, 2021b. Sentinel-1 Algorithms. URL: https://developers.google.com/earth-engine/guides/sentinel1.

Gorelick, N., Hancher, M., Dixon, M., Ilyushchenko, S., Thau, D., Moore, R., 2017. Google Earth Engine: Planetary-scale geospatial analysis for everyone. Remote Sens. Environ. 202, 18–27. https://doi.org/10.1016/j.rse.2017.06.031. URL: https://linkinghub.elsevier.com/retrieve/pii/S0034425717302900.

Grohmann, C.H., 2015. Effects of spatial resolution on slope and aspect derivation for regional-scale analysis. Comput. Geosci. 77, 111–117. https://doi.org/10.1016/j.cageo.2015.02.003. URL: https://linkinghub.elsevier.com/retrieve/pii/S0098300415000254.

Hansen, M.C., Loveland, T.R., 2012. A review of large area monitoring of land cover change using Landsat data. Remote Sens. Environ. 122, 66–74. https://doi.org/10.1016/j.rse.2011.08.024. URL: https://linkinghub.elsevier.com/retrieve/pii/S0034425712000314.

Hanssen, R.F., 2001. Radar Interferometry: Data Interpretation and Error Analysis. volume 2 of Remote Sensing and Digital Image Processing. Springer, Netherlands, Dordrecht. doi:10.1007/0-306-47633-9. URL: http://link.springer.com/10.1007/0-306-47633-9.

Haque, U., Blum, P., da Silva, P.F., Andersen, P., Pilz, J., Chalov, S.R., Malet, J.P., Auflic, M.J., Andres, N., Poyiadji, E., Lamas, P.C., Zhang, W., Peshevski, I., Pétursson, H.G., Kurt, T., Dobrev, N., García-Davalillo, J.C., Halkia, M., Ferri, S., Gaprindashvili, G., Engström, J., Keellings, D., 2016. Fatal landslides in Europe. Landslides 13, 1545–1554. https://doi.org/10.1007/s10346-016-0689-3. URL: http://link.springer.com/10.1007/s10346-016-0689-3.

Harris, C.R., Millman, K.J., van der Walt, S.J., Gommers, R., Virtanen, P., Cournapeau, D., Wieser, E., Taylor, J., Berg, S., Smith, N.J., Kern, R., Picus, M., Hoyer, S., van Kerkwijk, M.H., Brett, M., Haldane, A., del Río, J.F., Wiebe, M., Peterson, P., Gérard-Marchant, P., Sheppard, K., Reddy, T., Weckesser, W., Abbasi, H., Gohlke, C., Oliphant, T.E., 2020. Array programming with NumPy. Nature 585, 357–362. https://doi.org/10.1038/s41586-020-2649-2. URL: https://www.nature.com/articles/s41586-020-2649-2.

Herrera, G., Gutiérrez, F., García-Davalillo, J., Guerrero, J., Notti, D., Galve, J., Fernández-Merodo, J., Cooksley, G., 2013. Multi-sensor advanced DInSAR monitoring of very slow landslides: the Tena Valley case study (Central Spanish Pyrenees). Remote Sens. Environ. 128, 31–43. https://doi.org/10.1016/j.rse.2012.09.020. URL: https://linkinghub.elsevier.com/retrieve/pii/S003442571200380X.

Hilley, G.E., Bürgmann, R., Ferretti, A., Novali, F., Rocca, F., 2004. Dynamics of slow-moving landslides from permanent scatterer analysis. Science 304, 1952–1955. https://doi.org/10.1126/science.1098821. URL: http://www.sciencemag.org/cgi/doi/10.1126/science.1098821.

Hooper, A., 2008. A multi-temporal InSAR method incorporating both persistent scatterer and small baseline approaches. Geophys. Res. Lett. 35 https://doi.org/10.1029/2008GL034654. URL: https://agupubs.onlinelibrary.wiley.com/doi/abs/10.1029/2008GL034654.

Horn, B., 1981. Hill shading and the reflectance map. Proc. IEEE 69, 14–47. https://doi.org/10.1109/PROC.1981.11918. URL: http://ieeexplore.ieee.org/document/1456186/.

Hungr, O., Leroueil, S., Picarelli, L., 2014. The Varnes classification of landslide types, an update. Landslides 11, 167–194. https://doi.org/10.1007/s10346-013-0436-y. URL: http://link.springer.com/10.1007/s10346-013-0436-y.

Hunter, J.D., 2007. Matplotlib: A 2D Graphics Environment. Comput. Sci. Eng. 9, 90–95. https://doi.org/10.1109/MCSE.2007.55. URL: http://ieeexplore.ieee.org/document/4160265/.

Husár, L., Švaral, P., Janák, J., 2017. About the geometry of the Earth geodetic reference surfaces. J. Geometry Phys. 120, 192–207. https://doi.org/10.1016/j.geomphys.2017.05.016. URL: https://linkinghub.elsevier.com/retrieve/pii/S0393044017301389.

Intrieri, E., Carlà, T., Gigli, G., 2019. Forecasting the time of failure of landslides at slope-scale: A literature review. Earth-Sci. Rev. 193, 333–349. https://doi.org/10.1016/j.earscirev.2019.03.019. URL: https://linkinghub.elsevier.com/retrieve/pii/S001282521830518X.

Intrieri, E., Frodella, W., Raspini, F., Bardi, F., Tofani, V., 2020. Using satellite interferometry to infer landslide sliding surface depth and geometry. Remote Sens. 12, 1462. https://doi.org/10.3390/rs12091462. URL: https://www.mdpi.com/2072-4292/12/9/1462.

Intrieri, E., Raspini, F., Fumagalli, A., Lu, P., Del Conte, S., Farina, P., Allievi, J., Ferretti, A., Casagli, N., 2018. The Maoxian landslide as seen from space: detecting precursors of failure with Sentinel-1 data. Landslides 15, 123–133. https://doi.org/10.1007/s10346-017-0915-7. URL: http://link.springer.com/10.1007/s10346-017-0915-7.

Jaboyedoff, M., Oppikofer, T., Abellán, A., Derron, M.H., Loye, A., Metzger, R., Pedrazzini, A., 2012. Use of LiDAR in landslide investigations: a review. Nat. Hazards 61, 5–28. https://doi.org/10.1007/s11069-010-9634-2. URL: http://link.springer.com/10.1007/s11069-010-9634-2.

Japan Aerospace Exploration Agency, Earth Observation Research Center, 2019. ALOS Global Digital Surface Model (DSM) Product Description. Technical Report. Japan Aerospace Exploration Agency (JAXA).

Jordahl, K., van den Bossche, J., Fleischmann, M., Wasserman, J., McBride, J., Gerard, J., Tratner, J., Perry, M., Garcia Badaracco, A., Farmer, C., Geir Arne Hjelle, Snow, A.D., Cochran, M., Gillies, S., Culbertson, L., Bartos, M., Eubank, N., maxalbert, Bilogur, A., Rey, S., Ren, C., Arribas-Bel, D., Wasser, L., Wolf, L.J., Journois, M., Wilson, J., Greenhall, A., Holdgraf, C., Filipe, Leblanc, F., 2020. GeoPandas. doi:10.5281/zenodo.2585848. URL: doi: 10.5281/zenodo.2585848, software package.

Komac, M., Holley, R., Mahapatra, P., van der Marel, H., Bavec, M., 2015. Coupling of GPS/GNSS and radar interferometric data for a 3D surface displacement monitoring of landslides. Landslides 12, 241–257. https://doi.org/10.1007/s10346-014-0482-0. URL: http://link.springer.com/10.1007/s10346-014-0482-0.

Lacroix, P., Bièvre, G., Pathier, E., Kniess, U., Jongmans, D., 2018. Use of Sentinel-2 images for the detection of precursory motions before landslide failures. Remote Sens. Environ.

Lam, S.K., Pitrou, A., Seibert, S., 2015. Numba: a LLVM-based Python JIT compiler. In: Proceedings of the Second Workshop on the LLVM Compiler Infrastructure in HPC. Association for Computing Machinery, Austin, Texas. pp. 1–6. doi:10.1145/2833157.2833162. URL: doi: 10.1145/2833157.2833162.

Lauknes, T., Piyush Shanker, A., Dehls, J., Zebker, H., Henderson, I., Larsen, Y., 2010. Detailed rockslide mapping in northern Norway with small baseline and persistent scatterer interferometric SAR time series methods. Remote Sens. Environ. 114, 2097–2109. https://doi.org/10.1016/j.rse.2010.04.015. URL: https://linkinghub.elsevier.com/retrieve/pii/S0034425710001288.

van Leijen, F.J., 2014. Persistent Scatterer Interferometry based on geodetic estimation theory. PhD thesis. Delft University of Technology. doi:10.4233/uuid:5dba48d7-ee26-4449-b674-caa8df93e71e. URL: http://resolver.tudelft.nl/uuid:5dba48d7-ee26-4449-b674-caa8df93e71e, iSBN: 9789461862990 OCLC: 905870982.

Logar, J., Turk, G., Marsden, P., Ambrožic, T., 2017. Prediction of rainfall induced landslide movements by artificial neural networks. Nat. Hazards Earth Syst. Sci. Discuss. 1–18. https://doi.org/10.5194/nhess-2017-253. URL: https://www.nat-hazards-earth-syst-sci-discuss.net/nhess-2017-253/.

Mansour, M.F., Morgenstern, N.R., Martin, C.D., 2011. Expected damage from displacement of slow-moving slides. Landslides 8, 117–131. https://doi.org/10.1007/s10346-010-0227-7.

Massey, C., Petley, D., McSaveney, M., 2013. Patterns of movement in reactivated landslides. Eng. Geol. 159, 1–19. https://doi.org/10.1016/j.enggeo.2013.03.011. URL: https://linkinghub.elsevier.com/retrieve/pii/S0013795213000896.

Mondini, A., Santangelo, M., Rocchetti, M., Rossetto, E., Manconi, A., Monserrat, O., 2019. Sentinel-1 SAR amplitude imagery for rapid landslide detection. Remote Sens. 11, 760. https://doi.org/10.3390/rs11070760. URL: https://www.mdpi.com/2072-4292/11/7/760.

van Natijne, A.L., Bogaard, T.A., van Leijen, F.J., Hanssen, R.F., Lindenbergh, R.C., 2021. World-wide InSAR sensitivity index for landslide deformation tracking. URL: doi: 10.4121/14095777. data set.

van Natijne, A.L., Lindenbergh, R.C., Bogaard, T.A., 2020. Machine Learning: new potential for local and regional deep-seated landslide nowcasting. Sensors 20, 1425. https://doi.org/10.3390/s20051425. URL: https://www.mdpi.com/1424-8220/20/5/1425.

Notti, D., Davalillo, J.C., Herrera, G., Mora, O., 2010. Assessment of the performance of X-band satellite radar data for landslide mapping and monitoring: Upper Tena Valley case study. Nat. Hazards Earth Syst. Sci. 10, 1865–1875. https://doi.org/10.5194/nhess-10-1865-2010. URL: https://nhess.copernicus.org/articles/10/1865/2010/.

Notti, D., Herrera, G., Bianchini, S., Meisina, C., García-Davalillo, J.C., Zucca, F., 2014. A methodology for improving landslide PSI data analysis. Int. J. Remote Sens. 35, 2186–2214. https://doi.org/10.1080/01431161.2014.889864. URL: https://www.tandfonline.com/doi/abs/10.1080/01431161.2014.889864.

Notti, D., Meisina, C., Zucca, F., Colombo, A., 2011. Models to predict Persistent Scatterers data distribution and their capacity to register movement along the slope. In: Fringe Workshop 2011.

Novellino, A., Cigna, F., Brahmi, M., Sowter, A., Bateson, L., Marsh, S., 2017. Assessing the feasibility of a national InSAR ground deformation map of Great Britain with Sentinel-1. Geosciences 7, 19. https://doi.org/10.3390/geosciences7020019. URL: http://www.mdpi.com/2076-3263/7/2/19.

Peyret, M., Djamour, Y., Rizza, M., Ritz, J.F., Hurtrez, J.E., Goudarzi, M., Nankali, H., Chéry, J., Le Dortz, K., Uri, F., 2008. Monitoring of the large slow Kahrod landslide in Alborz mountain range (Iran) by GPS and SAR interferometry. Eng. Geol. 100, 131–141. https://doi.org/10.1016/j.enggeo.2008.02.013. URL: https://linkinghub.elsevier.com/retrieve/pii/S0013795208000616.

Pfeiffer, J., Zieher, T., Schmieder, J., Rutzinger, M., Strasser, U., 2021. Spatio-temporal assessment of the hydrological drivers of an active deep-seated gravitational slope deformation: The Vögelsberg landslide in Tyrol (Austria). Earth Surface Process. Landforms 1–17. https://doi.org/10.1002/esp.5129. URL: https://onlinelibrary.wiley.com/doi/10.1002/esp.5129.

Pinel, V., Poland, M., Hooper, A., 2014. Volcanology: Lessons learned from Synthetic Aperture Radar imagery. J. Volcanol. Geothermal Res. 289, 81–113. https://doi.org/10.1016/j.jvolgeores.2014.10.010. URL: https://linkinghub.elsevier.com/retrieve/pii/S0377027314003084.

Plank, S., Singer, J., Minet, C., Thuro, K., 2012. Pre-survey suitability evaluation of the differential synthetic aperture radar interferometry method for landslide monitoring. Int. J. Remote Sens. 33, 6623–6637. https://doi.org/10.1080/01431161.2012.693646. URL: https://www.tandfonline.com/doi/full/10.1080/01431161.2012.693646.

Plank, S., Singer, J., Thuro, K., Minet, C., 2010. The suitability of the differential radar interferometry method for deformation monitoring of landslides—a new GIS based evaluation tool. In: Geologically Active. Taylor & Francis Group, Auckland, New Zealand, pp. 2345–2352.

van Rossum, G., Python contributors, 2008. Python programming language. URL: https://www.python.org. software package.

Schlögel, R., Doubre, C., Malet, J.P., Masson, F., 2015. Landslide deformation monitoring with ALOS/PALSAR imagery: a D-InSAR geomorphological interpretation method. Geomorphology 231, 314–330. https://doi.org/10.1016/j.geomorph.2014.11.031. URL: https://linkinghub.elsevier.com/retrieve/pii/S0169555X14006254.

Schubert, A., Small, D., 2016. Sentinel-1A Radiometric Consistency between TOPS SLC and GRD Products. Technical Report UZH-S1-TOPS-RADIOMETRY-TN05. University of Zurich.

Segalini, A., Carri, A., Valletta, A., Martino, M., 2019. Innovative monitoring tools and early warning systems for risk management: a case study. Geosciences 9, 62. URL: http://www.mdpi.com/2076-3263/9/2/62, doi:10.3390/geosciences9020062.

Singleton, A., Li, Z., Hoey, T., Muller, J.P., 2014. Evaluating sub-pixel offset techniques as an alternative to D-InSAR for monitoring episodic landslide movements in vegetated terrain. Remote Sens. Environ. 147, 133–144. https://doi.org/10.1016/j.rse.2014.03.003. URL: https://linkinghub.elsevier.com/retrieve/pii/S0034425714000686.

Stumpf, A., Malet, J.P., Delacourt, C., 2017. Correlation of satellite image time-series for the detection and monitoring of slow-moving landslides. Remote Sens. Environ. 189, 40–55.

Sun, Q., Zhang, L., Ding, X., Hu, J., Li, Z., Zhu, J., 2015. Slope deformation prior to Zhouqu, China landslide from InSAR time series analysis. Remote Sens. Environ.

156, 45–57. https://doi.org/10.1016/j.rse.2014.09.029. URL: https://linkinghub.elsevier.com/retrieve/pii/S0034425714003836.

Tadono, T., Ishida, H., Oda, F., Naito, S., Minakawa, K., Iwamoto, H., 2014. Precise Global DEM Generation by ALOS PRISM. ISPRS Annals of Photogrammetry. Remote Sens. Spatial Inform. Sci. II-4 71–76. https://doi.org/10.5194/isprsannals-II-4-71-2014. URL: http://www.isprs-ann-photogramm-remote-sens-spatial-inf-sci.net/II-4/71/2014/.

Teunissen, P., 2000. Testing Theory: An Introduction, 1st. Delft University Press.

Tofani, V., Segoni, S., Agostini, A., Catani, F., Casagli, N., 2013. Technical Note: Use of remote sensing for landslide studies in Europe. Nat. Hazards Earth Syst. Sci. 13, 299–309. https://doi.org/10.5194/nhess-13-299-2013. URL: https://nhess.copernicus.org/articles/13/299/2013/.

Yin, Y., Zheng, W., Liu, Y., Zhang, J., Li, X., 2010. Integration of GPS with InSAR to monitoring of the Jiaju landslide in Sichuan, China. Landslides 7, 359–365. https://doi.org/10.1007/s10346-010-0225-9. URL: http://link.springer.com/10.1007/s10346-010-0225-9.

Zieher, T., Bremer, M., Rutzinger, M., Pfeiffer, J., Fritzmann, P., Wichmann, V., 2019. Assessment of landslide-induced displacement and deformation of above-ground objects using UAV-borne and airborne laser scanning data. ISPRS Annals of Photogrammetry, Remote Sensing and Spatial. Information Sci. IV-2/W5, 461–467. https://doi.org/10.5194/isprs-annals-IV-2-W5-461-2019. URL: https://www.isprs-ann-photogramm-remote-sens-spatial-inf-sci.net/IV-2-W5/461/2019/.